remote sensing

MDPI

Article

Synchronized and Co-Located Ionospheric and Atmospheric Anomalies Associated with the 2023 *Mw* 7.8 Turkey Earthquake

Syed Faizan Haider [1,†], Munawar Shah [1,2,†], Bofeng Li [2], Punyawi Jamjareegulgarn [3,*], José Francisco de Oliveira-Júnior [4] and Changyu Zhou [2]

[1] Space Education and GNSS Laboratory, National Center of GIS & Space Applications and Department of Space Science, Institute of Space Technology, Islamabad 44000, Pakistan; munawar@tongji.edu.cn (M.S.)
[2] College of Surveying and Geo Informatics, Tongji University, Shanghai 200070, China
[3] King Mongkut's Institute of Technology Ladkrabang, Prince of Chumphon Campus, Chumphon 86160, Thailand
[4] Laboratório de Meteorologia Aplicada e Meio Ambiente (LAMMA), Instituto de Ciências Atmosféricas (ICAT), Universidade Federal do Alagoas (UFAL), Maceio 57072-260, Brazil
* Correspondence: punyawi.ja@kmitl.ac.th
† These authors contributed equally to this work.

Abstract: Earth observations from remotely sensed data have a substantial impact on natural hazard surveillance, specifically for earthquakes. The rapid emergence of diverse earthquake precursors has led to the exploration of different methodologies and datasets from various satellites to understand and address the complex nature of earthquake precursors. This study presents a novel technique to detect the ionospheric and atmospheric precursors using machine learning (ML). We examine the multiple precursors of different spatiotemporal nature from satellites in the ionosphere and atmosphere related to the Turkey earthquake on 6 February 2023 (*Mw* 7.8), in the form of total electron content (TEC), land surface temperature (LST), sea surface temperature (SST), air pressure (AP), relative humidity (RH), outgoing longwave radiation (OLR), and air temperature (AT). As a confutation analysis, we also statistically observe datasets of atmospheric parameters for the years 2021 and 2022 in the same epicentral region and time period as the 2023 Turkey earthquake. Moreover, the aim of this study is to find a synchronized and co-located window of possible earthquake anomalies by providing more evidence with standard deviation (STDEV) and nonlinear autoregressive network with exogenous inputs (NARX) models. It is noteworthy that both the statistical and ML methods demonstrate abnormal fluctuations as precursors within 6 to 7 days before the impending earthquake over the epicenter. Furthermore, the geomagnetic anomalies in the ionosphere are detected on the ninth day after the earthquake ($Kp > 4$; $Dst < -70$ nT; $ap > 50$ nT). This study indicates the relevance of using multiple earthquake precursors in a synchronized window from ML methods to support the lithosphere–atmosphere–ionosphere coupling (LAIC) phenomenon.

Keywords: atmospheric precursors; GNSS TEC; LAIC; machine learning; remote sensing

check for updates

Citation: Haider, S.F.; Shah, M.; Li, B.; Jamjareegulgarn, P.; de Oliveira-Júnior, J.F.; Zhou, C. Synchronized and Co-Located Ionospheric and Atmospheric Anomalies Associated with the 2023 *Mw* 7.8 Turkey Earthquake. *Remote Sens.* **2024**, *16*, 222. https://doi.org/10.3390/rs16020222

Academic Editors: Xuemin Zhang, Chieh-Hung Chen, Yongxin Gao and Katsumi Hattori

Received: 1 December 2023
Revised: 28 December 2023
Accepted: 3 January 2024
Published: 5 January 2024

1. Introduction

Earthquakes take place as a result of tectonic stress accumulation, and these tectonic stresses result in the brittle failure of the lithospheric layers. Earthquakes occur because of tectonic stress changes inside the Earth's lithosphere at various hypo-central depths: low, intermediate, and deep extents [1,2]. The application of global navigation satellite system (GNSS) and remote sensing (RS) satellites has provided great insights into the monitoring of a possible earthquake precursor at different altitudes over the seismic zone before the occurrence of future main shocks [3–5]. Previous reports have used remotely sensed data to investigate possible seismic anomalies by studying the various aspects of earthquake energy evaluations from epicentral regions using satellite observations with different spatiotemporal datasets before and after the earthquake day [6–9]. Moreover, in various investigations, the GNSS and other RS satellites have found irregularities before large-magnitude and shallow-depth earthquakes above the epicenter during the seismogenic preparation period, enabling a comprehensive definition of seismic precursors [10–13]. Previous findings have relied on different RS data to observe the evolution of the earthquake energy in a close environment with the coupling phenomenon of the lithosphere, atmosphere, and ionosphere. For high-magnitude global earthquakes, these short-term irregularities can be seen 5–10 days prior to and 10 days after the main earthquake. However, there is still no clear demarcation of seismic precursors with remotely sensed data to clearly depict the location and occurrence of an earthquake event on a specific day. The seismic-induced anomalies exhibit positive and negative deviations beyond the prescribed bounds in various data of the lithosphere, atmosphere, and ionosphere [14,15]. The lithosphere experiences numerous geophysical changes as the earthquake's energy first interacts with this layer, generating possible precursors around the epicentral region of the earthquake [16]. During the seismic preparation phase, earthquake precursors may be monitored with many satellites at an altitude above the epicentral area, measuring the data of LST, SST, and other geophysical changes [17]. The atmospheric precursors from satellite data can also be observed in the form of ozone (O_3), nitrogen dioxide (NO_2), OLR, RH, AT, and AP associated with the main shock, which cause the composition of the lower atmosphere to vary and can further drift to the upper ionosphere [18–20]. Moreover, acoustic waves and atmospheric gravity waves (AGW) are produced by ground motion deformation and gas emissions [21–23]. Atmospheric ULF/ELF and VLF/LF (lower ionospheric perturbation) are considered earthquake precursors and viable options for short-term earthquake prediction [24]. Furthermore, earthquake anomalies can travel up to the ionosphere and the resulting precursors can be studied using the data of the GNSS for TEC, electron density, electric field variations, and other indices from satellite data [25,26]. The LAIC model explains exactly how earthquake anomalies can travel through several pathways in the atmosphere, followed by their travel to the upper ionosphere [27,28]. The precursors in the ionosphere and atmosphere can be merged in association with future earthquakes as induced by positive holes (p-holes) around the main shock regions during the preparation period [29]. In addition to p-holes, radon emission can generate seismic irregularities by air ionization in the atmosphere and be emitted to the upper atmosphere and ionosphere [30]. Furthermore, air anomalies may be caused by the emission of gases like radon, caused by tectonic stress changes and the deformation of rocks [31,32].

The intensity of atmospheric and ionospheric anomalies can vary in response to the depth, magnitude, and geophysical position of the earthquake [33]. The appearance of particular characteristics in earthquake anomalies can occur within days, hours, or even minutes before the main shock [34,35].

Earthquake anomalies have been investigated in many ways, using various statistical and mathematical techniques to establish a LAIC coupling hypothesis [36,37]. For example, Tronin [1] observed the anomalies 4–20 days prior to the earthquake in the form of LST increments. Furthermore, Hafeez et al. [38] observed the anomalous window for LST increments between 5 and 7 days prior to and 2 to 4 days after the earthquake. In association with other atmospheric anomalies from satellite data, a major increment in OLR was observed on the 13th day before the 2008 Wenchuan, China, earthquake [39]. Venkatanathan et al. [18] also identified OLR abnormalities in a statistical analysis of 10 earthquakes in India and its neighboring countries in 2012. Furthermore, Shah et al. [33] observed a synchronized pattern of LAIC through the coupling of variations in OLR and other satellites and ground datasets within 5–10 days prior to an earthquake. The atmospheric anomalies occurred due to tectonic movement around the epicenter to generate the ionization and thermodynamic processes, followed by irregularities in AT, RH, and AP changes. Khan et al. [40] observed a chain of significant increments in AT and a decrease in RH in 8 days before the 2021 Haiti earthquake. Additionally, Draz et al. [10] analyzed the atmospheric precursors in SST, AT, OLR, and RH within the anomalous window of 5–7 days before the 2021 Japan earthquake. Both positive and negative variations are observed in various variables, such as SST, TEC, and other atmospheric constituents, to form a mutual coupling system [41]. However, a significant research gap remains regarding the development of precise and reliable early warning systems, particularly in identifying specific precursors or patterns to accurately forecast the timing, location, and magnitude of earthquakes. Additionally, the integration of various data sources and their training by machine learning models for improved accuracy can be a significant area of advancement in this field.

In this study, we used various methods in the form of statistical and machine learning procedures to investigate the precursors of the *Mw* 7.8 Turkey earthquake event on TEC from GNSS satellites and atmospheric variables like RH, OLR, AP, SST, LST, and AT. Previous studies of this event [9,13] have only focused on ionospheric anomalies, but this work identifies synchronized and co-located ionospheric as well as atmospheric variations on the same day associated with the earthquake. Similarly, we study the significant pre- and/or post-seismic anomalies with reliable evidence from different remotely sensed datasets. The paper is organized as follows. Section 2 describes the area of study. Moreover, the data and methods are explained in Section 3. Section 4 describes the results and Section 5 presents the discussion. The conclusions are summarized in Section 6.

2. Area of Study

An earthquake of *Mw* 7.8 struck Southern Turkey on 6 February 2023 at 01:17:34 UTC (LT = UTC + 03:00 = 04:17:34). The epicenter was located at the geographical location of 37.2°N and 37.1°E at a shallow depth of 10 km (Figure 1). The earthquake data are provided by the United States Geological Survey (USGS) via https://www.usgs.gov/programs/earthquake-hazards (accessed on 15 May 2023). This earthquake caused massive destruction to property and more than 70,000 people were exposed to destructive landslides. Furthermore, this earthquake was caused by a shallow strike–slip fault. More tectonic and technical information about this earthquake can be found on the USGS website.

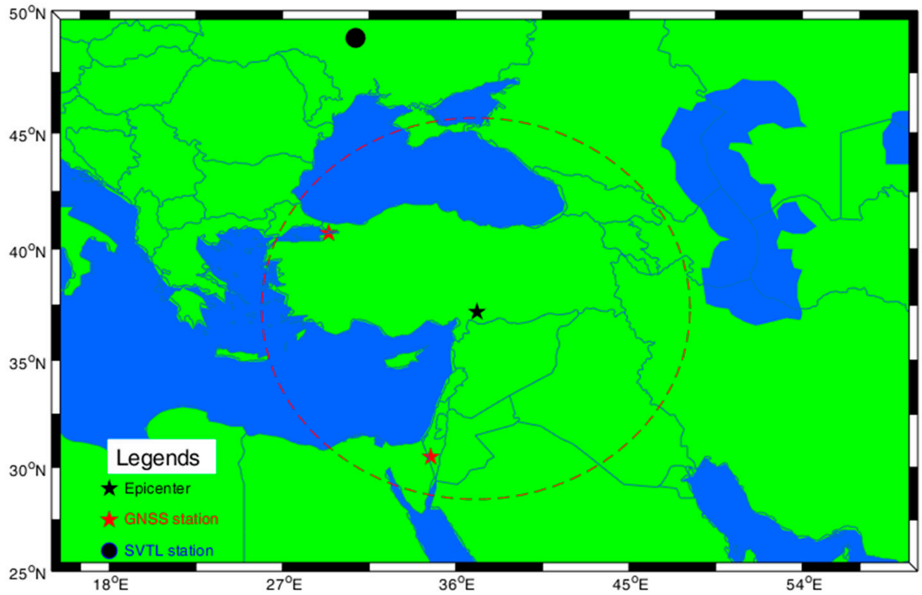

Figure 1. The location of the 2023 *Mw* 7.8 Turkey earthquake, indicated by a black filled star. The red filled stars indicated the GNSS stations and the black filled circle indicates the SVTL station outside the preparation zone. The red dashed circle represents the earthquake-impacted region.

3. Data and Methods

3.1. Data

For this study, we analyzed various atmospheric and ionospheric parameters over 30 days (19 days prior to and 10 days after of the earthquake) to identify a synchronized and co-located precursory pattern. For this purpose, the atmospheric anomalies averaged over epicenter in the region of 28°N to 44°N in latitude and 27°E to 48°E in longitude for the year 2023 were observed in time series for anomalies. We also observed the datasets of atmospheric parameters for the same region and same time period as the Turkey earthquake for the previous 5 years (2018–2022) as a confutation analysis. Similarly, the OLR, RH, AP, and AT datasets for the Turkey earthquake were acquired from NOAA PSL, via https://psl.noaa.gov/ (last accessed on 20 May 2023). The OLR, RH, AP, and AT data were retrieved in a daily temporal resolution with spatial coverage of 2.5° × 2.5° in latitude × longitude, respectively.

The daily SST data for this study were retrieved from the Japan Aerospace Exploration Agency (JAXA) via the webpage https://global.jaxa.jp/projects/sat/gcom_w/ (accessed on 10 June 2023). Moreover, the SST data had global coverage and a spatial resolution of 15 km along the swath. On the other hand, the LST data from MODIS correlated considerably with in situ surface temperature observations [33,38]. In this study, the daily LST data from the MODIS (Terra) satellite were obtained from https://modis.gsfc.nasa.gov/data/ (retrieved on 12 June 2023). Moreover, the MODIS data had a diurnal pattern in 36 spectral bands for the whole globe, with a swath width of 2330 km.

Furthermore, the GNSS TEC is widely utilized to study ionospheric anomalies associated with earthquakes across the globe [4,10,42], and the geomagnetic indices showed storm time variations, derived from the NASA OMNIWeb via https://omniweb.gsfc.nasa.gov/form/dx1.html (retrieved on 15 June 2023). The ionospheric anomalies were studied from the TEC of three IGS stations, with two stations, TUBI and RAMO, located inside the main shock area and the third station, SVTL, located beyond the main shock preparation area (Table 1). We retrieved the TEC of the SVTL station to validate and separate the ionospheric variations due to geomagnetic storms and monitor the real earthquake-induced ionospheric deviations. The TEC data from all three GNSS stations were obtained via http://www.ionolab.org/ (accessed on 15 June 2023). Additionally, the ionospheric precursors for the Turkey earthquake were analyzed from the vertical TEC (VTEC). The VTEC is calculated using the slant TEC (STEC) and is measured in TEC units (1 TECU = 10^{16} el/m^2) [43].

$$STEC_a^h = \frac{-(f_1^2\, f_2^2)}{40.3\,(f_1^2 - f_2^2)}\left(P^h_{(4,\,a)} - c.DCB_a - c.DCB^h\right) \quad (1)$$

$$VTEC = STEC \times cos\left[arcsin\left(\frac{Rsinz}{R+H}\right)\right] \quad (2)$$

Table 1. List of GNSS stations.

No.	Station Name	Distance from Epicenter (km)	Coordinates		Country
			Latitude	Longitude	
1	TUBI	764	40.7°N	29.4°E	Turkey
2	RAMO	776	30.5°N	34.7°E	Israel
3	SVTL	2640	60.5°N	29.7°E	Russia

In Equation (1), (f_1^2, f_2^2) are the dual frequencies, $P^h_{(4,\,a)}$ is the variation among the smoothed coded measurements, and DCB^h and DCB_a are the differential code biases. Similarly, c represents the speed of light. Furthermore, R is the radius of the Earth, z is the zenith angle, and H represents the ionospheric pierce point height (for this study, we considered it as 320 km).

3.2. Methods

The synchronized and co-located atmospheric and ionospheric anomalies using both the statistical and ML methods were studied using the standard deviation (STDEV) method. Moreover, the NARX method was used to confirm the anomalies associated with the main shock as an ML procedure. Multiple parameters were analyzed over the epicenter within the Dobrovolsky region [44], where the impacted area in kms can be determined using the below equation.

$$R = 10^{0.43Mw} \tag{3}$$

In the above equation, R is the earthquake stress radius in kms and Mw is the magnitude of the forthcoming earthquake. The stress radius of the Turkey (Mw 7.8) earthquake was approximately 2259 km, as calculated by the Dobrovolsky formula.

3.2.1. Statistical Method

We examined any variation in the multiple datasets associated with the seismic event beyond the upper and lower confidence limits by calculating the mean (M) and standard deviation (STDEV) for the data retrieved over the epicentral zone of the Dobrovolsky region. We also applied the statistical method to the atmospheric parameters for the years 2021 and 2022 to check and validate the variations from the 2023 Turkey earthquake-induced anomalies. For the time series analysis of multiple earthquake precursors, we implemented a threshold limit of two standard deviations (2 × STDEV), which has already been employed in previous studies to determine earthquake precursors from satellite data [10,26,32]. This bounds method can clearly distinguish a substantial and co-located anomaly from the other unclear anomalies. The confidence limits are calculated by the below equations.

$$UB = M + 2 \times STDEV \tag{4}$$

$$LB = M - 2 \times STDEV \tag{5}$$

The above equations can confirm the earthquake-induced anomalies beyond the upper and below the lower bound as abnormal seismic precursors. Furthermore, the deviation from either above or below the confidence bound is plotted as the deviation.

3.2.2. NARX

The NARX method is widely employed to detect the specific nature of deviations related to seismic events during the preparation period [38,40,45]. The expression below is the NARX model equation.

$$y(t) = f\left(y(t-1), y(t-2), \ldots, y\left(t-n_y\right), x(t-1), x(t-2), \ldots, x(t-n_x)\right) \tag{6}$$

The network algorithm and training prediction error for a nonlinear function f can be obtained by the output, hidden layer count, input delays, activation functions, associated neurons, and learning technique. To start the prediction process, N observations, y_1, y_2, . . ., y_N, are selected as a training set, while the remaining ones, y_{N+1}, y_{N+2}, . . ., y_{N+m}, are selected as a test set. The inputs are the mean value, respective time, observed values, and the deviation of the observed values from the confidence limits. The daily predicted values are obtained as the output layer. The suggested network's training model can be seen in Figure 2 below.

$$y_4 = f(y_1, y_2, y_3, t_1, t_2, t_3) \tag{7}$$

$$y_5 = f(y_2, y_3, y_4, t_2, t_3, t_4) \tag{8}$$

$$y_N = f(y_{N-3}, y_{N-2}, y_{N-1}, t_{N-3}, t_{N-2}, t_{N-1}) \tag{9}$$

The prediction error (PE) is reduced by finding the optimum weights in the prediction performance. The PE equation is shown below.

$$PE = \sum_{k-0}^{N} (\hat{y}(t-k) - y(t-k)). \tag{10}$$

where $\hat{y}$ is the network's output. The testing patterns are given in the below equations.

$$y_{N+4} = f(y_{N+1}, y_{N+2}, y_{N+3}, t_{N+1}, t_{N+2}, t_{N+3}) \tag{11}$$

$$y_{N+5} = f(y_{N+2}, y_{N+3}, y_{N+4}, t_{N+2}, t_{N+3}, t_{N+4}) \tag{12}$$

$$y_{N+m} = f(y_{N+m-3}, y_{N+m-2}, y_{N+m-1}, t_{N+m-3}, t_{N+m-2}, t_{N+m-1}) \tag{13}$$

Subsequently, the deviations are computed by analyzing the variations among the NARX-estimated and the observed values of the pre-defined confidence limits [38,46].

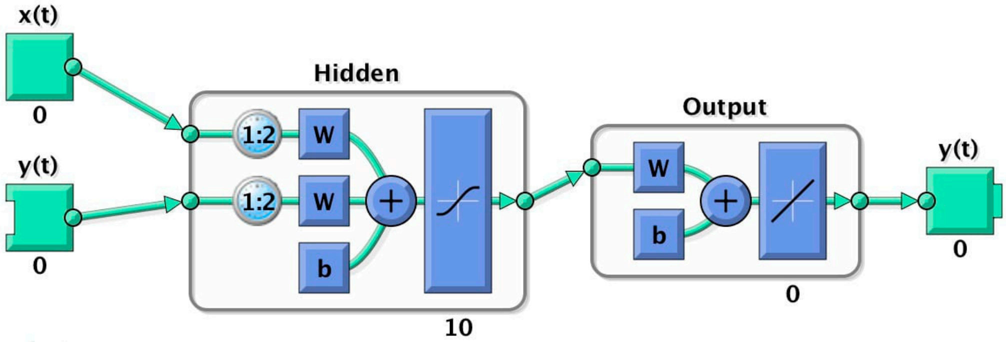

Figure 2. Flow chart diagram of the NARX neural network.

4. Results

We implemented the statistical and machine learning approaches to examine precursory values in various atmospheric and ionospheric datasets for possible seismic precursors related to the Turkey earthquake. The deviations were thoroughly examined and discussed in detail. The deviations in the daily OLR values over the preparation zone of the Turkey earthquake are shown in Figure 3. We found no possible variations in the time series data of the OLR for the years 2021 and 2022 (Figure 3a,b). However, a positive anomaly of 4.6 W/m^2 was observed on the 6th day prior to the earthquake in the year 2023 (Figure 3d). To quantify the atmospheric variations, we examined the variations in the daily RH values over the epicentral region of the Turkey earthquake (Figure 4). The RH values for the years 2021 and 2022 over the same region and same time period as the Turkey earthquake showed no possible RH anomalies (Figure 4a,b). On the other hand, we found a negative deviation of 0.5% on the 7th day prior to the main shock in the earthquake preparation period (Figure 4d). The anomalous trend in RH remained for 2 days and a significant deviation of −4.1% occurred on the 6th day prior to the main shock.

Moreover, we analyzed the variations in the daily AP values over the epicentral region of the Turkey earthquake (Figure 5). The observed values for the years 2021 and 2022 showed no clear deviations for the AP dataset as compared to the year 2023 for the earthquake (Figure 5a,b). For the earthquake year in 2023, we found a negative anomaly of 0.51 kPa on the 6th day prior to the earthquake (Figure 5d). Furthermore, the NARX-estimated OLR values displayed clear variations on the 6th and 7th days prior to the seismic event (Figure 6a). The deviations on the 6th and 7th days were 7.1 W/m^2 and 19.5 W/m^2 from the NARX-predicted values, respectively (Figure 6b).

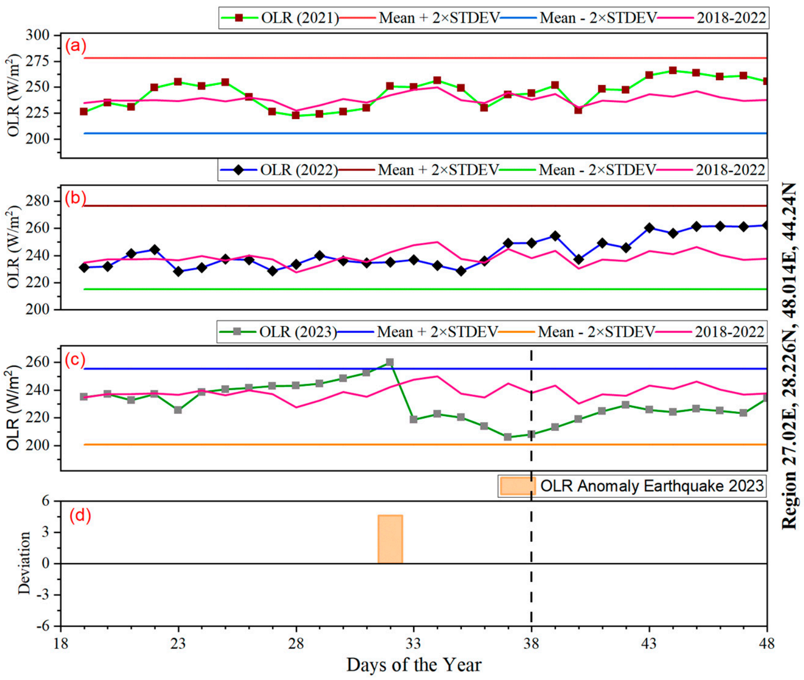

Figure 3. (**a**) The OLR time series data of 30 days with upper and lower bounds for the year 2021, where the solid pink line represents the OLR mean value for the 5 years between 2018 and 2022 as a confutation analysis. (**b**) Daily OLR values with bounds for the year 2022. (**c**) Daily OLR variable with bounds for the year 2023. (**d**) Deviation of OLR from the pre-defined confidence bounds for the 2023 Turkey earthquake. The black dashed line depicts the main shock day.

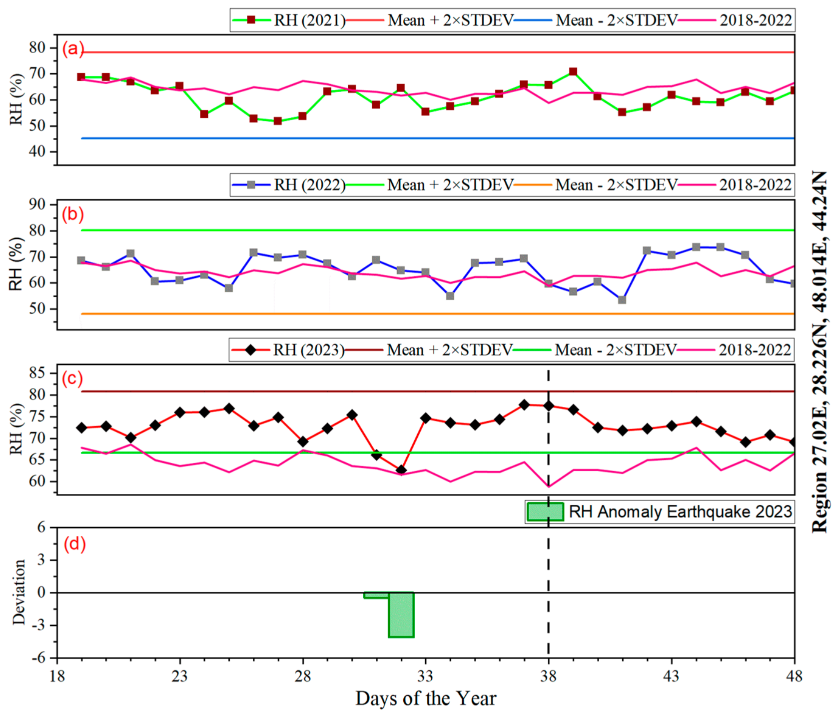

Figure 4. (**a**) The RH time series data over the epicentral region of the Turkey earthquake for 30 days with upper and lower bounds for the year 2021. (**b**) Daily RH values with bounds for the year 2022. (**c**) Daily data of RH variable with bounds for the year 2023. (**d**) Deviation of RH from the pre-defined confidence bounds for the 2023 Turkey earthquake. The black dashed line depicts the main shock day.

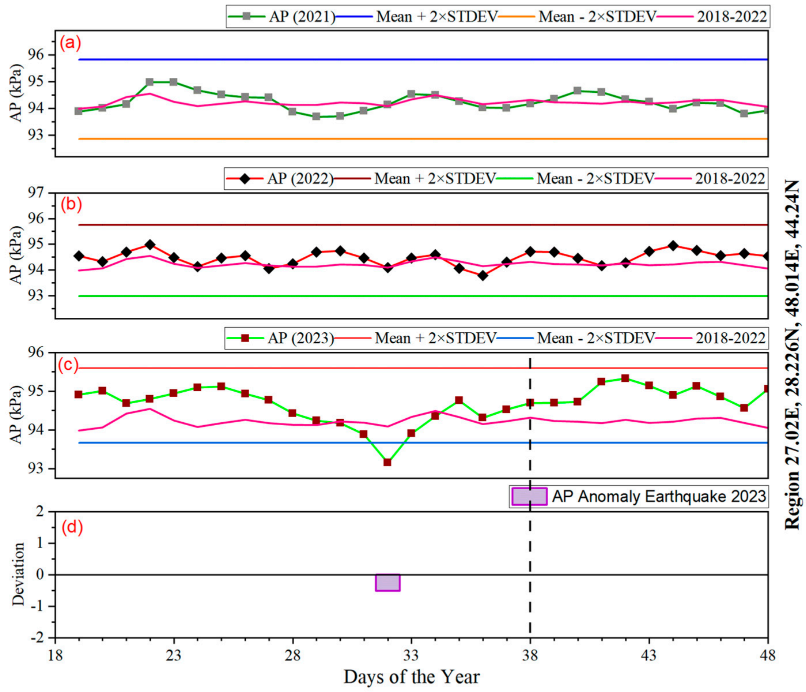

Figure 5. (**a**) The time series of AP data over the epicentral region of the Turkey earthquake with upper and lower bounds for the year 2021. (**b**) Daily AP values of 30 days with bounds for the year 2022. (**c**) Daily data of AP variable with bounds for the year 2023. (**d**) Deviation of AP from the pre-defined confidence bounds for the 2023 Turkey earthquake. The black dashed line depicts the main shock day.

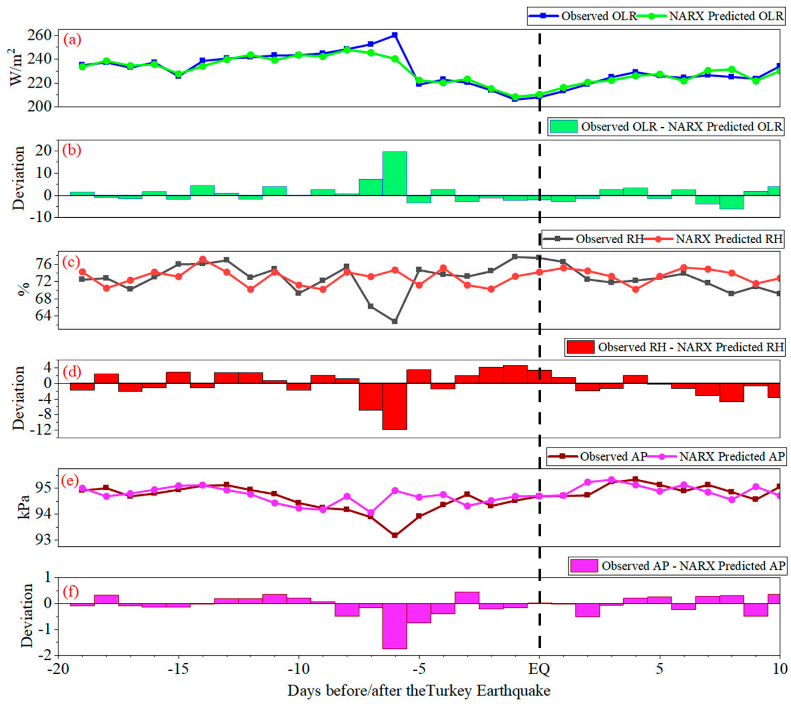

Figure 6. The deviations between the calculated and NARX-estimated datasets of atmospheric variables: (**a**) observed OLR data and NARX-estimated OLR data, (**b**) deviations of NARX-estimated OLR data from the observed OLR data, (**c**) calculated RH data and NARX-estimated RH data, (**d**) deviations of NARX-estimated RH data from the calculated RH data, (**e**) observed AP values and NARX-estimated AP values, (**f**) deviations of NARX-estimated AP data from the calculated AP data. The black dashed line represents the main event.

Furthermore, the variations in the NARX-estimated RH values displayed prominent negative deviations within 6–7 days before the main seismic event (Figure 6c). We detected deviations of −7% and −12% from the NARX-predicted values on the 6th and 7th day, respectively (Figure 6d). Furthermore, the NARX-estimated AP values displayed clear deviations on the 6th day prior to the seismic event (Figure 6e). The observed deviation on the 6th day was −1.75 kPa from the NARX-predicted value (Figure 6f).

In this study, we also analyzed the deviations in the daily AT values from satellites over the epicentral region of the Turkey earthquake (Figure 7). We observed no possible AT anomalies over the same region as the Turkey earthquake for the years 2021 and 2022 (Figure 7a,b). However, a positive anomaly of 3.26 K could be seen on the 6th day prior to the earthquake day (Figure 7d).

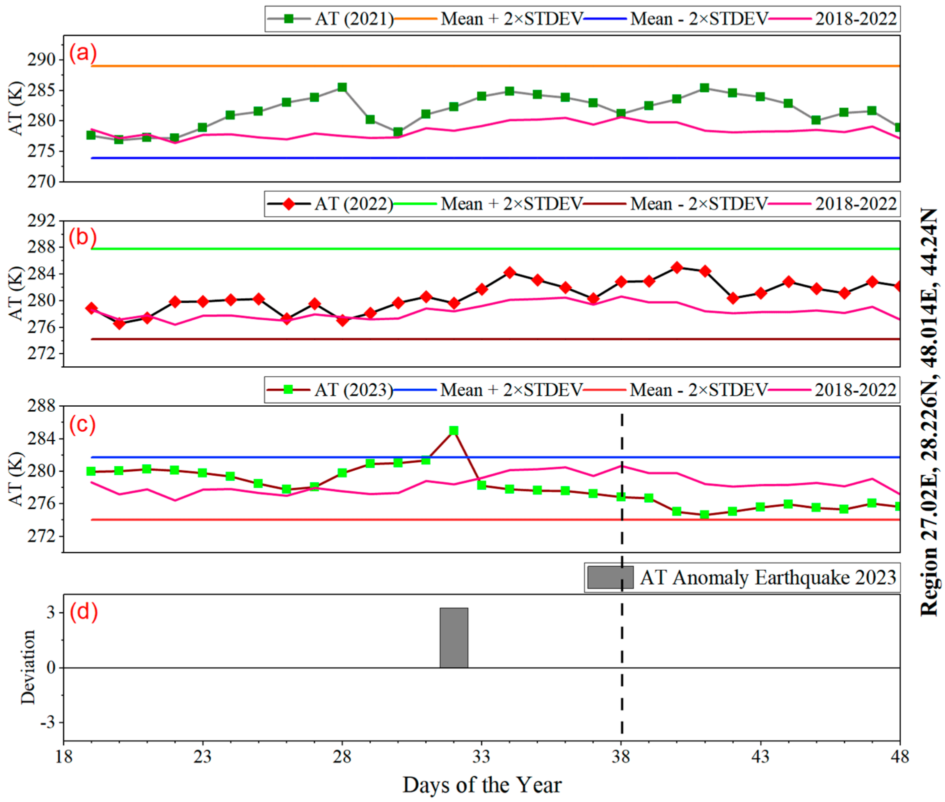

Figure 7. (**a**) The AT time series data of 30 days with the upper and lower bounds for the year 2021 as a confutation analysis. (**b**) Daily AT values with bounds for the year 2022. (**c**) Daily data of AT variable with bounds for the year 2023. (**d**) Deviation of AT from the pre-defined confidence bounds for the 2023 Turkey earthquake. The black dashed line depicts the main shock day.

To further provide stringent proof of the atmospheric precursors, we examined the daily SST values from remotely sensed satellite for the years 2021, 2022, and the earthquake year of 2023 (Figure 8). The variations in the daily SST values over the impacted area of the Turkey earthquake showed no abnormal time series data of SST for the years 2021 and 2022 (Figure 8a,b). Moreover, the time series data showed an obvious negative anomaly of 1.6 K on the 7th day prior to the 2023 earthquake (Figure 8d). On the other hand, the analyses of the daily LST values over the impacted zone of the Turkey earthquake are shown in Figure 9. The LST data of the years 2021 and 2022 showed no deviation over the epicentral region for the same time period (Figure 9a,b). However, we observed a clear positive anomaly of 0.8 K on the 7th day prior to the earthquake (Figure 9d). The anomalous trend remained for 2 days and showed a deviation of 2.1 K on the 6th day prior to the main shock.

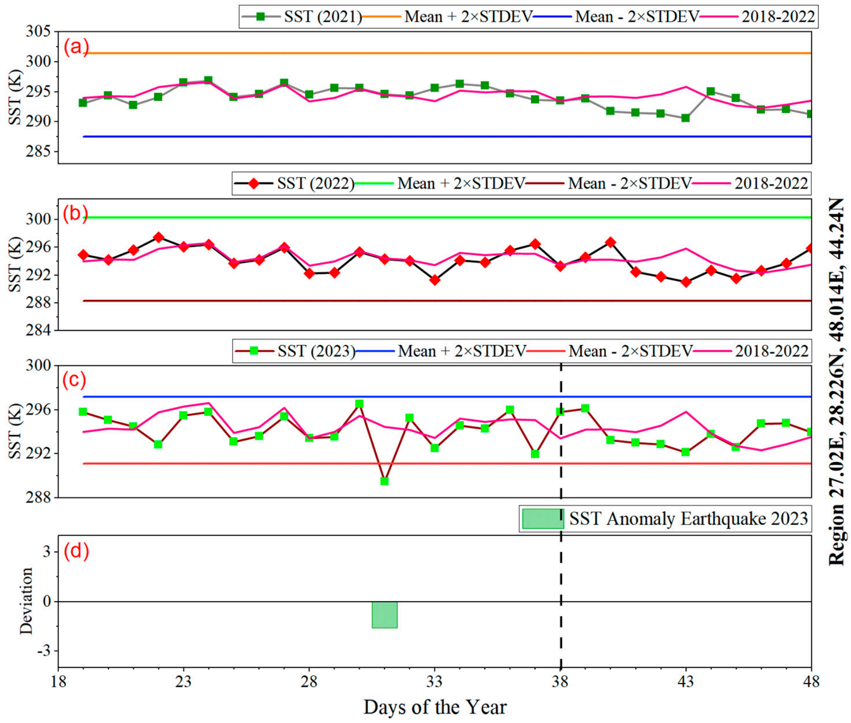

Figure 8. (**a**) The SST time series data over the epicentral region of the Turkey earthquake for 30 days with upper and lower bounds for the year 2021. (**b**) Daily SST values with bounds for the year 2022. (**c**) Daily data of SST variable with bounds for the year 2023. (**d**) Deviation of SST from predefined confidence bounds for the 2023 Turkey earthquake. The black dashed line depicts the main shock day.

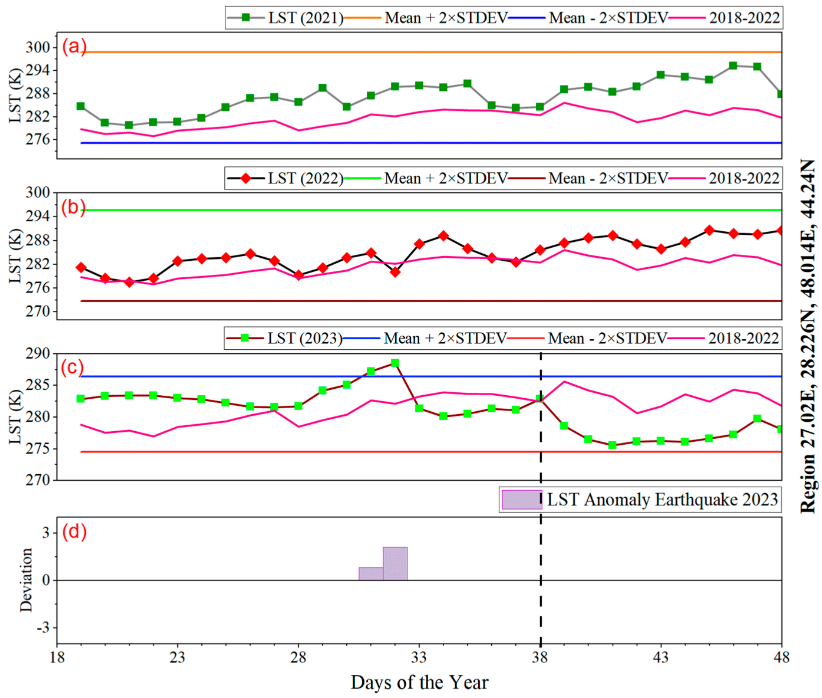

Figure 9. (**a**) The time series LST data over the epicentral region of the Turkey earthquake with upper and lower bounds for the year 2021. (**b**) Daily LST values of 30 days with bounds for the year 2022. (**c**) Daily data of LST variable with bounds for the year 2023. (**d**) Deviation of LST from the predefined confidence bounds for the 2023 Turkey earthquake. The black dashed line depicts the main shock day.

Furthermore, the variations in the NARX-estimated AT values displayed clear anomalies within a 6–7 day window prior to the seismic event (Figure 10a). We observed clear deviations of 2.3 K and 6.7 K from the NARX-predicted values on the 6th and 7th day, respectively (Figure 10b). Additionally, the NARX-estimated SST values displayed clear deviations on the 7th day prior to the seismic event (Figure 10c). We detected a clear variation of −6.7 K from the NARX-predicted value (Figure 10d). We observed clear variations in the NARX-estimated LST data as positive variations within 6–7 days prior to the main event (Figure 10e); specifically, we detected variations of 5.7 and 7.1 K from the NARX-estimated values (Figure 10f).

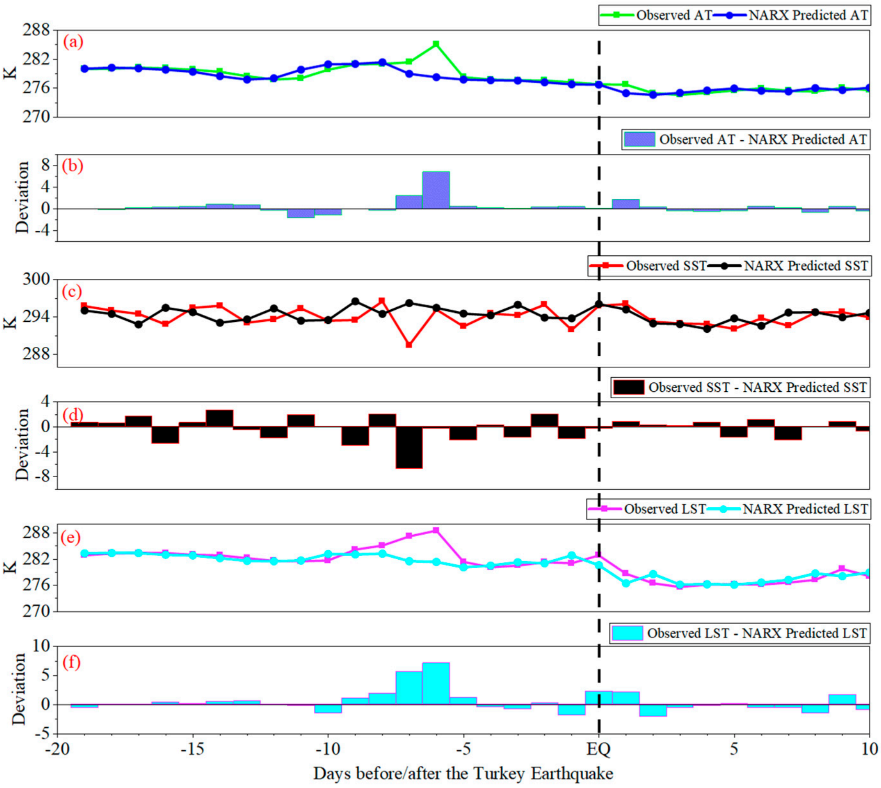

Figure 10. The variations between the calculated and NARX-estimated datasets of atmospheric variables: (**a**) calculated AT values and NARX-estimated AT values, (**b**) deviations of NARX-estimated AT data from calculated AT data, (**c**) calculated SST data and NARX-estimated SST data, (**d**) deviations of NARX-estimated SST data from observed SST data, (**e**) observed LST data and NARX-estimated LST data, (**f**) deviations of NARX-estimated LST data from calculated LST data. The black dashed line depicts the main event.

In this study, the TEC values retrieved from the two GNSS stations (TUBI and RAMO) within the preparation area of the *Mw* 7.8 Turkey event displayed clear seismic variations. Furthermore, the GNSS TEC data from the IGS station (SVTL) outside the earthquake-impacted area were utilized for the confirmation of either the earthquake- or geomagnetic storm-induced anomalies. We observed positive variations 7 and 6 days prior to the major event in both the TUBI and RAMO stations' values, in the absence of active storm conditions (Figure 11). The TEC retrieved from the TUBI station displayed positive anomalies of 7.6 and 3.9 TECU on the 7th and 6th day prior to the earthquake, respectively (Figure 11d). Moreover, the RAMO station's values displayed positive anomalies of 9.5 and 5.4 TECU on the 7th and 6th day prior to the earthquake, respectively (Figure 11e). However, the STVL station showed no TEC deviation during the quiet storm days. On the other hand, positive TEC deviations were observed on the 9th day after the seismic event in the data of the SVTL station, as shown in Figure 11f. Additionally, positive VTEC variations occurred in all three IGS stations (TUBI, RAMO, and SVTL) on the 9th day after the earthquake, associated with active geomagnetic storm days.

The NARX-estimated VTEC also displayed clear variations for all three IGS stations during storm days (Figure 12d). Moreover, the NARX-estimated values displayed clear variations in VTEC values at 6–7 days prior to the major event in two GNSS stations (TUBI and RAMO) (Figure 12). In this study, various atmospheric and ionospheric parameters showed deviations in both the statistical and ML methods for the 2023 Turkey earthquake. All observed ionospheric and atmospheric deviations are listed in Tables 2 and 3.

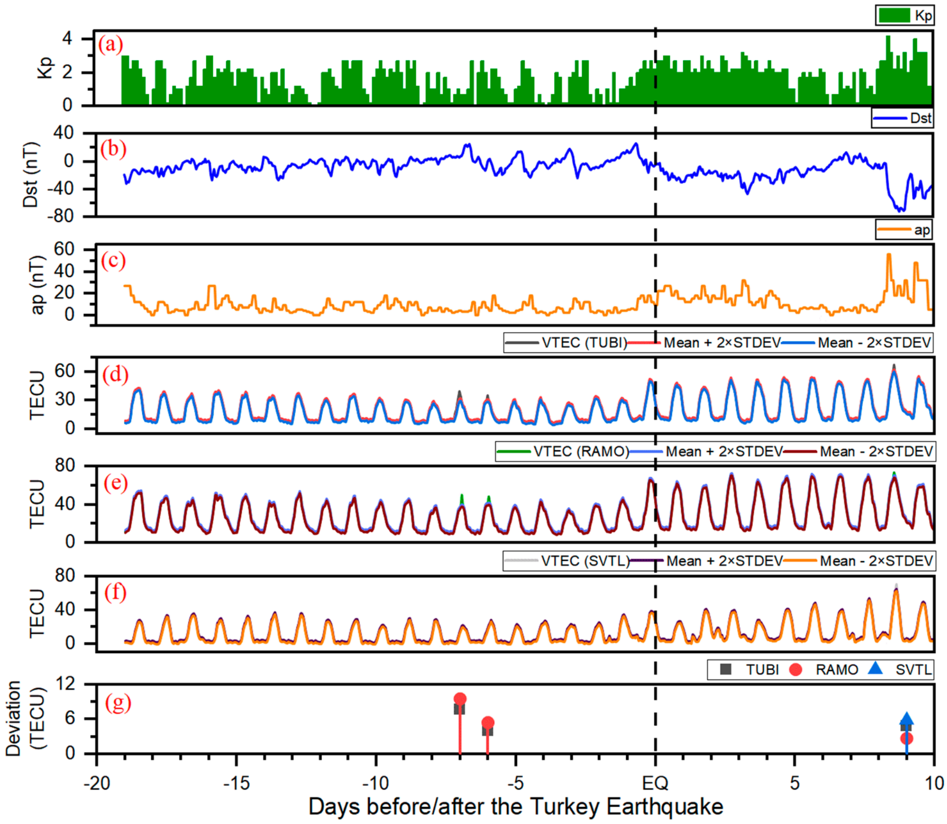

Figure 11. The geomagnetic storm indices in the form of (**a**) Kp, (**b**) Dst, (**c**) ap, (**d**) statistical analysis of TUBI VTEC with bounds, (**e**) RAMO station values with upper and lower bounds, (**f**) time series data of SVTL VTEC with bounds, (**g**) deviations of VTEC values for all the available stations (TUBI, RAMO, and SVTL). The black dashed line represents the main shock day.

Table 2. List of deviations detected using the statistical method.

Variable	Anomalous Days	Deviation from Bounds
OLR	−6	4.6 W/m^2
RH	−7, −6	−0.5, −4.1%
AP	−6	−0.51 kPa
AT	−6	3.26 K
SST	−7	−1.6 K
LST	−7, −6	0.8, 2.1 K
TEC (TUBI)	−7, −6, 9	7.6, 3.9, 4.8 TECU
TEC (RAMO)	−7, −6, 9	9.5, 5.4, 2.7 TECU
TEC (SVTL)	9	5.8 TECU

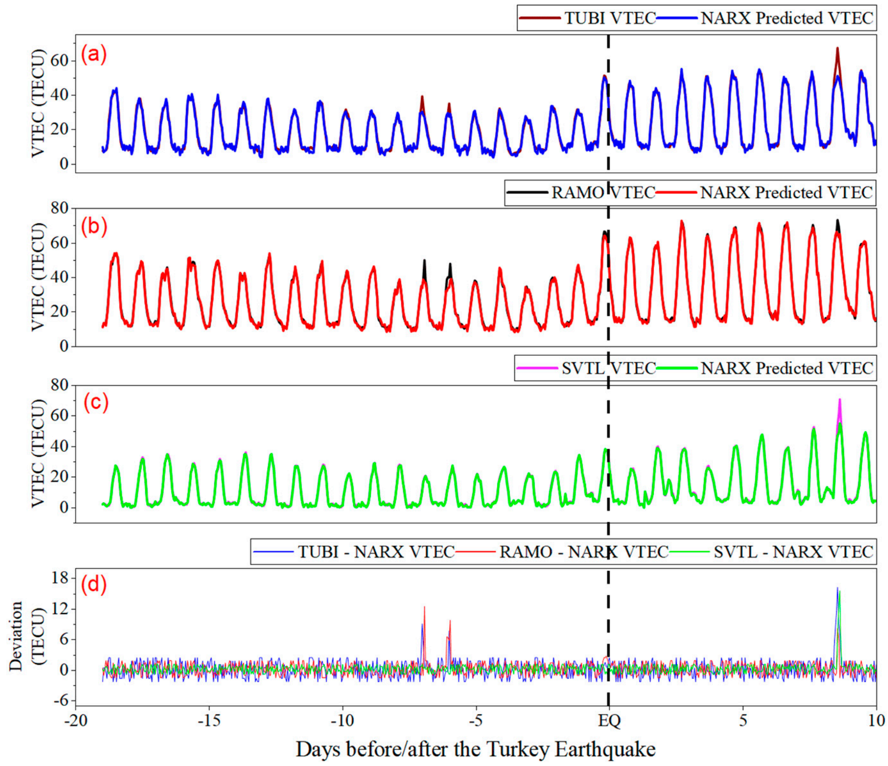

Figure 12. (**a**) The variations in VTEC values from TUBI station and NARX-estimated VTEC values, (**b**) variations in RAMO VTEC values and NARX-estimated VTEC values, (**c**) variations in SVTL VTEC values and NARX-estimated VTEC values, (**d**) deviations of NARX-estimated VTEC values from TUBI, RAMO, and SVTL VTEC values. The black dashed line is for the main event.

Table 3. List of anomalies detected with the NARX method.

Variable	Anomalous Days	Variation from NARX-Estimated Value
OLR	−7, −6	7.1, 19.5 W/m^2
RH	−7, −6	−7, −12%
AP	−6	−1.75 kPa
AT	−7, −6	2.3, 6.7 K
SST	−7	−6.7 K
LST	−7, −6	5.7, 7.1 K
TEC (TUBI)	−7, −6, 9	9.1, 7.7, 16.2 TECU
TEC (RAMO)	−7, −6, 9	12.5, 9.8, 8.2 TECU
TEC (SVTL)	9	15.5 TECU

5. Discussion

In this study, we observed the possible earthquake precursors to obtain an LAIC hypothesis by integrating multiple satellite variables for the *Mw* 7.8 Turkey earthquake using various methods. The earthquake developed precursory indications of deviation in different variables in the atmosphere and ionosphere in the Dobrovolsky region within a 6–7 day window before the earthquake. One can see the anomalous behavior of these parameters over the epicenter of the 2023 Turkey earthquake in our analyses.

We detected an immense increment in OLR over the epicenter for the Turkey earthquake (Figure 3c). We observed these variations due to massive energy release during the major event, as was suggested for the earthquake energy outflow into the atmosphere in previous reports [47]. The OLR is considered to be an essential parameter in forecasting the future main shocks because it reflects the earthquake energy in the atmosphere [48]. Furthermore, we noticed a considerable drop in RH in our investigation (Figure 4c), which was due to air ionization and thermal energy absorption, which changed the humidity and air temperature in the atmosphere (increasing the AT and reducing the RH), as suggested by Shah et al. [49]. An abrupt decrease in AP was observed, as shown in Figure 5c, as the AP fluctuated with the appearance of the seismic waves and reached a peak with the appearance of Rayleigh waves at the lithosphere–atmosphere interface as a response to the main shock pressure [50]. Furthermore, it created seismic waves that were pushed by the ground motion over the epicenter towards the atmosphere [50]. We also observed prominent positive fluctuations in AT as a result of the abrupt release of seismic energy prior to the main shock (Figure 7c). Previous reports have found that lower RH is associated with higher AT as a possible sign of seismic precursors [51]. On the other hand, air ionization alters RH, AT, and the surface temperature by increasing the outgoing infrared radiation [52]. The air ionization responses among the different atmospheric layers were altered due to massive stresses from the epicenter of the future earthquake [53]. Similarly, the gases released from the Earth's crust resulted in OLR deviations, followed by fluctuations in RH, AP, and AT, as well as air ionization [10,33,40]. The p-holes induced by the earthquake within the preparation zone can also alter the air ionization [54], and this increased the electrical conductivity in our case study. The deviations in OLR, RH, AP, and AT were also analyzed as indicators of future seismic events [55]. The use of statistical and machine learning methodologies to analyze the daily OLR, RH, AP, and AT in this study is a new approach to identifying variations associated with the main shock. These analyses confirmed the changes within the preparation zone of the 2023 Turkey earthquake as anomalous behavior beyond the bounds. We also observed a massive decrease in SST within the impacted area of the Turkey earthquake (Figure 8c). The SST measurements revealed significant evidence of disruption around the earthquake, which supported the investigation of additional atmospheric anomalies. The findings of this study, in the form of multiple precursory variations, are consistent with previous investigations [56]. We also observed a substantial enhancement in the LST over the epicenter of the Turkey earthquake (Figure 9c). This is likely due to radon and greenhouse gas emissions at the epicentral depth of strong earthquakes [33]. These gases flow to the ground and are mixed with atmospheric constituents to further affect the lower atmosphere and travel up to generate abnormalities in the ionosphere [16]. Moreover, electric charges can cause fluctuations in LST due to p-hole emission from the rocks under stress [57]. In this work, the anomalies on the 6th and 7th days prior to the main event were synchronized and co-located above the epicenter from the satellite data (Table 2). Furthermore, we also observed positive VTEC anomalies for three IGS stations operating inside, namely TUBI and RAMO, and outside, namely SVTL, the earthquake-impacted area during quiet as well as active storm days (Figure 11). The findings of VTEC anomalies in this work are consistent with the previously observed ionospheric variations from GNSS and other satellites [33,42]. It is possible that radon emission during the earthquake preparation phase causes these ionospheric VTEC anomalies [16]. On the other hand, the energetic alpha particles charged by the earthquake may raise the air conductivity via the radioactive decay of radon [58]. Furthermore, the LAIC phenomena described by numerical models of ionospheric ionization by the upward electric field over the epicenter support the findings of this work [59–61]. They also show the plasma flow from the epicenter as a source of increase and/or decrease in the ionospheric aspects above the epicenter. The multiple analyses performed for the LAIC hypothesis development found legitimate atmospheric and ionospheric anomalies associated with earthquakes [62–66]. The incorporation of machine learning also improved the credibility of the precursors to some extent by removing the biases in the data [67–71]. On the other hand, the need to integrate more data and their possible relations has still not been addressed, as in previous reports [72–75]. In this study, we observed substantial positive and negative deviations in multiple ionospheric and atmospheric parameters related to the *Mw* 7.8 Turkey earthquake; however, it is critical to note that high-resolution datasets and additional research are required to increase the quality of our results and to construct a more complete prediction model. Moreover, advanced ML approaches and the observation and analysis of multiple atmospheric and ionospheric precursors are required for precise estimations of the seismic precursors.

6. Conclusions

In this study, we found a synchronized and co-located pattern in various earthquake precursors related to the *Mw* 7.8 Turkey earthquake, from multiple atmospheric and GNSS observables, using statistical and ML techniques. We also studied the time series data of the atmospheric parameters for the years 2021 and 2022 as a confutation analysis. We found no deviations in the statistical analysis of the atmospheric parameters of past years. Moreover, the positive variations in OLR, AT, and LST and negative deviations in RH, AP, and SST indicated the integrated atmospheric correlations with the seismic event. Similarly, positive GNSS TEC anomalies were observed for both the TUBI and RAMO stations, and no anomalies were observed for the STVL station during the quite storm days. Under active geomagnetic conditions, the VTEC of all three GNSS stations showed positive anomalies in both the statistical and ML methods. The statistical and machine learning approaches used to study multiple parameters inside the earthquake zone showed significant precursors within a 6–7 day window prior to the Turkey earthquake. Although these anomalies indicate probable precursor behaviors with the current satellite data, we still need a more thorough understanding of the forecasting of earthquakes with more high-resolution data. To increase the earthquake forecasting accuracy with clear insights into lithosphere–atmosphere–ionosphere interactions, future research should focus on acquiring finer-grained data, analyzing new variables, and establishing advanced prediction models.

Author Contributions: Conceptualization, M.S.; writing—review and editing, S.F.H., M.S., B.L., P.J., J.F.d.O.-J. and C.Z. All authors have read and agreed to the published version of the manuscript.

Funding: This research received no external funding.

Data Availability Statement: The authors have no permission to share the data. However, most of the data are publicly available.

Conflicts of Interest: The authors declare no conflicts of interest.

References

1. Tronin, A. Remote Sensing and Earthquakes: A Review. *Phys. Chem. Earth* **2006**, *31*, 138–142. [CrossRef]
2. Lu, K.; Hou, M.; Jiang, Z.; Wang, Q.; Sun, G.; Liu, J. Understanding Earthquake from the Granular Physics Point of View-Causes of Earthquake, Earthquake Precursors and Predictions. *Int. J. Mod. Phys. B* **2018**, *32*, 1850081. [CrossRef]
3. Sun, R.; Wang, J.; Cheng, Q.; Mao, Y.; Ochieng, W.Y. A New IMU-Aided Multiple GNSS Fault Detection and Exclusion Algorithm for Integrated Navigation in Urban Environments. *GPS Solut.* **2021**, *25*, 147. [CrossRef]
4. Pikridas, C.; Bitharis, S.; Katsougiannopoulos, S.; Spanakaki, K.; Karolos, I.-A. Study of TEC Variations Using Permanent Stations GNSS Data in Relation with Seismic Events. Application on Samothrace Earthquake of 24 May 2014. *Geod. Cartogr.* **2019**, *45*, 137. [CrossRef]
5. Jiao, Z.; Shan, X. Pre-Seismic Temporal Integrated Anomalies from Multiparametric Remote Sensing Data. *Remote Sens.* **2022**, *14*, 2343. [CrossRef]
6. Xiong, P.; Shen, X.H.; Bi, Y.X.; Kang, C.L.; Chen, L.Z.; Jing, F.; Chen, Y. Study of Outgoing Longwave Radiation Anomalies Associated with Haiti Earthquake. *Nat. Hazards Earth Syst. Sci.* **2010**, *10*, 2169–2178. [CrossRef]
7. Akyol, A.A.; Arikan, O.; Arikan, F. A Machine Learning-Based Detection of Earthquake Precursors Using Ionospheric Data. *Radio Sci.* **2020**, *55*, 1–21. [CrossRef]
8. Dong, W.; Yang, Y.; Qu, J.; Xiao, S.; Li, Y. Local Information-Enhanced Graph-Transformer for Hyperspectral Image Change Detection with Limited Training Samples. *IEEE Trans. Geosci. Remote Sens.* **2023**, *61*, 5509814. [CrossRef]
9. Vesnin, A.; Yasyukevich, Y.; Perevalova, N.; Şentürk, E. Ionospheric Response to the 6 February 2023 Turkey–Syria Earthquake. *Remote Sens.* **2023**, *15*, 2336. [CrossRef]
10. Draz, M.U.; Shah, M.; Jamjareegulgarn, P.; Shahzad, R.; Hasan, A.M.; Ghamry, N.A. Deep Machine Learning Based Possible Atmospheric and Ionospheric Precursors of the 2021 Mw 7.1 Japan Earthquake. *Remote Sens.* **2023**, *15*, 1904. [CrossRef]
11. Carter, B.A.; Kellerman, A.C.; Kane, T.A.; Dyson, P.L.; Norman, R.; Zhang, K. Ionospheric Precursors to Large Earthquakes: A Case Study of the 2011 Japanese Tohoku Earthquake. *J. Atmos. Sol. Terr. Phys.* **2013**, *102*, 290–297. [CrossRef]

12. Colonna, R.; Filizzola, C.; Genzano, N.; Lisi, M.; Tramutoli, V. Optimal Setting of Earthquake-Related Ionospheric TEC (Total Electron Content) Anomalies Detection Methods: Long-Term Validation over the Italian Region. *Geosciences* **2023**, *13*, 150. [CrossRef]
13. Maletckii, B.; Astafyeva, E.; Sanchez, S.A.; Kherani, E.A.; de Paula, E.R. The 6 February 2023 Türkiye Earthquake Sequence as Detected in the Ionosphere. *J. Geophys. Res. Space Phys.* **2023**, *128*, e2023JA031663. [CrossRef]
14. Adil, M.A.; Şentürk, E.; Pulinets, S.A.; Amory-Mazaudier, C. A Lithosphere–Atmosphere–Ionosphere Coupling Phenomenon Observed Before M 7.7 Jamaica Earthquake. *Pure Appl. Geophys.* **2021**, *178*, 3869–3886. [CrossRef]
15. Hafeez, A.; Shah, M.; Ehsan, M.; Jamjareegulgarn, P.; Ahmed, J.; Tariq, M.A.; Iqbal, S.; Naqvi, N.A. Possible Atmosphere and Ionospheric Anomalies of the 2019 Pakistan Earthquake Using Statistical and Machine Learning Procedures on MODIS LST, GPS TEC, and GIM TEC. *IEEE J. Sel. Top. Appl. Earth Obs. Remote Sens.* **2021**, *14*, 11126–11133. [CrossRef]
16. Pulinets, S.; Ouzounov, D. Lithosphere–Atmosphere–Ionosphere Coupling (LAIC) Model—An Unified Concept for Earthquake Precursors Validation. *J. Asian Earth Sci.* **2011**, *41*, 371–382. [CrossRef]
17. Shah, M.; Draz, M.U.; Saleem, T. A Comprehensive Study on the synchronized Outgoing Longwave Radiation and Relative Humidity Anomalies related to global Mw $\geq$ 6.5 Earthquakes. *Nat. Hazards* **2023**, *7*, 24–46. [CrossRef]
18. Venkatanathan, N.; Kaarthick, B.; Priyadharshini, C. OLR Anomalies Prior to Big Earthquakes (Mw > 6.0)-a Case Study on Earthquakes of India's Neighboring Region Occurred during the Year 2012. *New Concepts Glob. Tecton.* **2013**, *1*, 34–44.
19. Alvan, H.V.; Azad, F.H.; Mansor, S. Latent Heat Flux and Air Temperature Anomalies along an Active Fault Zone Associated with Recent Iran Earthquakes. *Adv. Space Res.* **2013**, *52*, 1678–1687. [CrossRef]
20. Mahmood, I.; Iqbal, M.F.; Shahzad, M.I.; Qaiser, S. Investigation of Atmospheric Anomalies Associated with Kashmir and Awaran Earthquakes. *J. Atmos. Sol. Terr. Phys.* **2017**, *154*, 75–85. [CrossRef]
21. De Santis, A.; Abbattista, C.; Alfonsi, L.; Amoruso, L.; Campuzano, S.A.; Carbone, M.; Cesaroni, C.; Cianchini, G.; De Franceschi, G.; De Santis, A.; et al. Geosystemics View of Earthquakes. *Entropy* **2019**, *21*, 412. [CrossRef] [PubMed]
22. Lizunov, G.; Skorokhod, T.; Hayakawa, M.; Korepanov, V. Formation of Ionospheric Precursors of Earthquakes—Probable Mechanism and Its Substantiation. *Open J. Earthq. Res.* **2020**, *9*, 142–169. [CrossRef]
23. Du, W.; Wang, G. Fully probabilistic seismic displacement analysis of spatially distributed slopes using spatially correlated vector intensity measures. *Earthq. Eng. Struct. Dyn.* **2014**, *43*, 661–679. [CrossRef]
24. Hayakawa, M.; Izutsu, J.; Schekotov, A.; Yang, S.-S.; Solovieva, M.; Budilova, E.; Nikolopoulos, D.; Martinez-Frias, J. Lithosphere-Atmosphere-Ionosphere Coupling Effects Based on Multiparameter Precursor Observations for February–March 2021 Earthquakes (M~7) in the Offshore of Tohoku Area of Japan. *Geosciences* **2021**, *11*, 481. [CrossRef]
25. Tariq, M.A.; Shah, M.; Hernández-Pajares, M.; Iqbal, T. Pre-Earthquake Ionospheric Anomalies before Three Major Earthquakes by GPS-TEC and GIM-TEC Data during 2015–2017. *Adv. Space Res.* **2019**, *63*, 2088–2099. [CrossRef]
26. Akhoondzadeh, M.; Parrot, M.; Saradjian, M.R. Electron and Ion Density Variations before Strong Earthquakes (M > 6.0) Using DEMETER and GPS Data. *Nat. Hazards Earth Syst. Sci.* **2010**, *10*, 7–18. [CrossRef]
27. Chen, J.; Wen, L.; Bi, C.; Liu, Z.; Liu, X.; Yin, L.; Zheng, W. Multifractal analysis of temporal and spatial characteristics of earthquakes in Eurasian seismic belt. *Open Geosci.* **2023**, *15*, 20220482. [CrossRef]
28. Zhou, G.; Zhang, H.; Xu, C.; Zhou, X.; Liu, Z.; Zhao, D.; Wu, G. A Real-Time Data Acquisition System for Single-Band Bathymetric LiDAR. *IEEE Trans. Geosci. Remote Sens.* **2023**, *61*, 5702721. [CrossRef]
29. Freund, F. Charge Generation and Propagation in Igneous Rocks. *J. Geodyn.* **2002**, *33*, 543–570. [CrossRef]
30. Yin, L.; Wang, L.; Ge, L.; Tian, J.; Yin, Z.; Liu, M.; Zheng, W. Study on the Thermospheric Density Distribution Pattern during Geomagnetic Activity. *Appl. Sci.* **2023**, *13*, 5564. [CrossRef]
31. Liu, X.; Zhang, Q.; Shah, M.; Hong, Z. Atmospheric-Ionospheric Disturbances Following the April 2015 Calbuco Volcano from GPS and OMI Observations. *Adv. Space Res.* **2017**, *60*, 2836–2846. [CrossRef]
32. Satti, M.S.; Ehsan, M.; Abbas, A.; Shah, M.; de Oliveira-Júnior, J.F.; Naqvi, N.A. Atmospheric and Ionospheric Precursors Associated with Mw$\geq$ 6.5 Earthquakes from Multiple Satellites. *J. Atmos. Sol. Terr. Phys.* **2022**, *227*, 105802. [CrossRef]
33. Shah, M.; Shahzad, R.; Jamjareegulgarn, P.; Ghaffar, B.; Oliveira-Júnior, J.F.d.; Hassan, A.M.; Ghamry, N.A. Machine-Learning-Based Lithosphere-Atmosphere-Ionosphere Coupling Associated with *Mw* > 6 Earthquakes in America. *Atmosphere* **2023**, *14*, 1236. [CrossRef]
34. Eleftheriou, A.; Filizzola, C.; Genzano, N.; Lacava, T.; Lisi, M.; Paciello, R.; Pergola, N.; Vallianatos, F.; Tramutoli, V. Long-Term RST Analysis of Anomalous TIR Sequences in Relation with Earthquakes Occurred in Greece in the Period 2004–2013. *Pure Appl. Geophys.* **2016**, *173*, 285–303. [CrossRef]
35. Su, Y.C.; Liu, J.Y.; Chen, S.P.; Tsai, H.F.; Chen, M.Q. Temporal and Spatial Precursors in Ionospheric Total Electron Content of the 16 October 1999 Mw7.1 Hector Mine Earthquake. *J. Geophys. Res. Space Phys.* **2013**, *118*, 6511–6517. [CrossRef]
36. Xiong, P.; Tong, L.; Zhang, K.; Shen, X.; Battiston, R.; Ouzounov, D.; Iuppa, R.; Crookes, D.; Long, C.; Zhou, H. Towards Advancing the Earthquake Forecasting by Machine Learning of Satellite Data. *Sci. Total Environ.* **2021**, *771*, 145256. [CrossRef]
37. Li, R.; Zhang, H.; Chen, Z.; Yu, N.; Kong, W.; Li, T.; Liu, Y. Denoising method of ground-penetrating radar signal based on independent component analysis with multifractal spectrum. *Measurement* **2022**, *192*, 110886. [CrossRef]
38. Hafeez, A.; Ehsan, M.; Abbas, A.; Shah, M.; Shahzad, R. Machine Learning-Based Thermal Anomalies Detection from MODIS LST Associated with the M_w 7.7 Awaran, Pakistan Earthquake. *Nat. Hazards* **2022**, *111*, 2097–2115. [CrossRef]

39. Jing, F.; Shen, X.H.; Kang, C.L.; Xiong, P. Variations of Multi-Parameter Observations in Atmosphere Related to Earthquake. *Nat. Hazards Earth Syst. Sci.* **2013**, *13*, 27–33. [CrossRef]
40. Khan, M.M.; Ghaffar, B.; Shahzad, R.; Khan, M.R.; Shah, M.; Amin, A.H.; Eldin, S.M.; Naqvi, N.A.; Ali, R. Atmospheric Anomalies Associated with the 2021 M w 7.2 Haiti Earthquake Using Machine Learning from Multiple Satellites. *Sustainability* **2022**, *14*, 14782. [CrossRef]
41. Shi, K.; Guo, J.; Liu, X.; Liu, L.; You, X.; Wang, F. Seismo-Ionospheric Anomalies Associated with Mw 7.8 Nepal Earthquake on 2015 April 25 from CMONOC GPS Data. *Geosci. J.* **2020**, *24*, 391–406. [CrossRef]
42. Abbasi, A.R.; Shah, M.; Ahmed, A.; Naqvi, N.A. Possible Ionospheric Anomalies Associated with the 2009 M_w 6.4 Taiwan Earthquake from DEMETER and GNSS TEC. *Acta Geod. Geophys.* **2021**, *56*, 77–91. [CrossRef]
43. Schaer, S.; Société Helvétique des Sciences Naturelles; Commission Géodésique. *Mapping and Predicting the Earth's Ionosphere Using the Global Positioning System*; Schweizerische Geodätische Kommission Zürich: Zürich, Switzerland, 1999; Volume 59.
44. Dobrovolsky, I.P.; Zubkov, S.I.; Miachkin, V.I. Estimation of the Size of Earthquake Preparation Zones. *Pure Appl. Geophys.* **1979**, *117*, 1025–1044. [CrossRef]
45. Nekoee, M.; Shah-Hosseini, R. Thermal Anomaly Detection Using NARX Neural Network Method to Estimate the Earthquake Occurrence Time. *Earth Obs. Geomat. Eng.* **2020**, *4*, 98–108. [CrossRef]
46. Nugroho, H.A.; Joelianto, E.; Widiyantoro, S. Time Series Estimation of Earthquake Occurrences in Bali and Its Surroundings Using NARX Network Model. In Proceedings of the 2013 3rd International Conference on Instrumentation, Control and Automation, ICA 2013, Ungasan, Indonesia, 28–30 August 2013; pp. 251–256.
47. Shah, M.; Jin, S.G. Statistical characteristics of seismo-ionospheric GPS TEC disturbances prior to global $Mw \geq 5.0$ earthquakes (1998–2014). *J. Geodyn.* **2015**, *92*, 42–49. [CrossRef]
48. Rawat, V.; Saraf, A.K.; Das, J.; Sharma, K.; Shujat, Y. Anomalous Land Surface Temperature and Outgoing Long-Wave Radiation Observations Prior to Earthquakes in India and Romania. *Nat. Hazards* **2011**, *59*, 33–46. [CrossRef]
49. Shah, M.; Tariq, M.A.; Naqvi, N.A. Atmospheric Anomalies Associated with Mw>6.0 Earthquakes in Pakistan and Iran during 2010–2017. *J. Atmos. Sol. Terr. Phys.* **2019**, *191*, 105056. [CrossRef]
50. Watada, S.; Kunugi, T.; Hirata, K.; Sugioka, H.; Nishida, K.; Sekiguchi, S.; Oikawa, J.; Tsuji, Y.; Kanamori, H. Atmospheric Pressure Change Associated with the 2003 Tokachi-Oki Earthquake. *Geophys. Res. Lett.* **2006**, *33*, L24306. [CrossRef]
51. Shah, M.; Calabia, A.; Tariq, M.A.; Ahmed, J.; Ahmed, A. Possible ionosphere and atmosphere precursory analysis related to Mw >6.0 earthquakes in Japan. *Remote Sens. Environ.* **2020**, *239*, 111620. [CrossRef]
52. Shah, M.; Ahmed, A.; Ehsan, M.; Khan, M.; Tariq, M.A.; Calabia, A.; Rahman, Z. Total electron content anomalies associated with earthquakes occurred during 1998–2019. *Acta Astronaut.* **2020**, *175*, 268–276. [CrossRef]
53. Troyan, V.N.; Hayakawa, M. Seismo Electromagnetics: Lithosphere-Atmosphere-Ionosphere Coupling. In *Seismo Electromagnetics: Lithosphere-Atmosphere-Ionosphere Coupling*; Terrapub: Tokyo, Japan, 2002.
54. Freund, F.T.; Takeuchi, A.; Lau, B.W.S.; Al-Manaseer, A.; Fu, C.C.; Bryant, N.A.; Ouzounov, D. Stimulated Infrared Emission from Rocks: Assessing a Stress Indicator. *eEarth* **2007**, *2*, 7–16. [CrossRef]
55. Walker, R.; Jackson, J. Offset and Evolution of the Gowk Fault, SE Iran: A Major Intra-Continental Strike-Slip System. *J. Struct. Geol.* **2002**, *24*, 1677–1698. [CrossRef]
56. Mohamed, E.K.; Elrayess, M.; Omar, K. Evaluation of Thermal Anomaly Preceding Northern Red Sea Earthquake, the 16th June 2020. *Arab. J. Sci. Eng.* **2022**, *47*, 7387–7406. [CrossRef]
57. Ouzounov, D.; Freund, F. Mid-Infrared Emission Prior to Strong Earthquakes Analyzed by Remote Sensing Data. *Adv. Space Res.* **2004**, *33*, 268–273. [CrossRef]
58. Ondoh, T. Anomalous Sporadic-E Layers Observed before M7. 2 Hyogo-Ken Nanbu Earthquake; Terrestrial Gas Emanation Model. *Adv. Polar Up. Atmos. Res.* **2003**, *17*, 96–108.
59. Kuo, C.L.; Huba, J.D.; Joyce, G.; Lee, L.C. Ionosphere Plasma Bubbles and Density Variations Induced by Pre-Earthquake Rock Currents and Associated Surface Charges. *J. Geophys. Res. Space Phys.* **2011**, *116*, A10317. [CrossRef]
60. Zhou, G.; Xu, J.; Hu, H.; Liu, Z.; Zhang, H.; Xu, C.; Zhao, Y. Off-Axis Four-Reflection Optical Structure for Lightweight Single-Band Bathymetric LiDAR. *IEEE Trans. Geosci. Remote Sens.* **2023**, *61*, 1000917. [CrossRef]
61. Shahzad, F.; Shah, M.; Riaz, S.; Ghaffar, B.; Ullah, I.; Eldin, S.M. Integrated Analysis of Lithosphere-Atmosphere-Ionospheric Coupling Associated with the 2021 M_w 7.2 Haiti Earthquake. *Atmosphere* **2023**, *14*, 347. [CrossRef]
62. Zhao, Z.; Xu, G.; Zhang, N.; Zhang, Q. Performance analysis of the hybrid satellite-terrestrial relay network with opportunistic scheduling over generalized fading channels. *IEEE Trans. Veh. Technol.* **2022**, *71*, 2914–2924. [CrossRef]
63. Wu, M.; Ba, Z.; Liang, J. A procedure for 3D simulation of seismic wave propagation considering source-path-site effects: Theory, verification and application. *Earthq. Eng. Struct. Dyn.* **2022**, *51*, 2925–2955. [CrossRef]
64. Ma, S.; Qiu, H.; Yang, D.; Wang, J.; Zhu, Y.; Tang, B.; Cao, M. Surface multi-hazard effect of underground coal mining. *Landslides* **2023**, *20*, 39–52. [CrossRef]
65. Zheng, B.; Lin, D.; Qi, S.; Hu, Y.; Jin, Y.; Chen, Q.; Yan, R. Turbulent skin-friction drag reduction by annular dielectric barrier discharge plasma actuator. *Phys. Fluids* **2023**, *35*, 125129. [CrossRef]
66. Yin, H.; Wu, Q.; Yin, S.; Dong, S.; Dai, Z.; Soltanian, M.R. Predicting mine water inrush accidents based on water level anomalies of borehole groups using long short-term memory and isolation forest. *J. Hydrol.* **2023**, *616*, 128813. [CrossRef]

67. Qasim, M.; Shah, M.; Shahzad, R.; Jamjareegulgarn, P. Atmospheric precursors from multiple satellites associated with the 2020 Mw 6.5 Idaho (USA) earthquake. *Adv. Space Res.* **2023**, *73*, 440–455. [CrossRef]
68. Morales, A.M.; Becerra, G.E.V.; Almaraz, J.R.M.; Felix, C.A.M.; Shah, M. Applying support vector machine (SVM) using GPS-TEC and Space Weather parameters to distinguish ionospheric disturbances possibly related to earthquakes. *Adv. Space Res.* **2023**, *72*, 4420–4434. [CrossRef]
69. Zhang, S.; Bai, X.; Zhao, C.; Tan, Q.; Luo, G.; Wang, J.; Xi, H. Global CO_2 Consumption by Silicate Rock Chemical Weathering: Its Past and Future. *Earth's Future* **2021**, *9*, e1938E–e2020E. [CrossRef]
70. Yin, L.; Wang, L.; Li, J.; Lu, S.; Tian, J.; Yin, Z.; Zheng, W. YOLOV4_CSPBi: Enhanced Land Target Detection Model. *Land* **2023**, *12*, 1813. [CrossRef]
71. Liu, Q.Y.; Li, D.Q.; Tang, X.S.; Du, W. Predictive Models for Seismic Source Parameters Based on Machine Learning and General Orthogonal Regression Approaches. *Bull. Seismol. Soc. Am.* **2023**, *113*, 2363–2376. [CrossRef]
72. Zhu, W.; Chen, J.; Sun, Q.; Li, Z.; Tan, W.; Wei, Y. Reconstructing of High-Spatial-Resolution Three-Dimensional Electron Density by Ingesting SAR-Derived VTEC into IRI Model. *IEEE Geosci. Remote Sens. Lett.* **2022**, *19*, 4508305. [CrossRef]
73. Zhou, G.; Zhao, D.; Zhou, X.; Xu, C.; Liu, Z.; Wu, G.; Zou, L. An RF Amplifier Circuit for Enhancement of Echo Signal Detection in Bathymetric LiDAR. *IEEE Sens. J.* **2022**, *22*, 20612–20625. [CrossRef]
74. Dong, W.; Zhao, J.; Qu, J.; Xiao, S.; Li, N.; Hou, S.; Li, Y. Abundance Matrix Correlation Analysis Network Based on Hierarchical Multihead Self-Cross-Hybrid Attention for Hyperspectral Change Detection. *IEEE Trans. Geosci. Remote Sens.* **2023**, *61*, 5501513. [CrossRef]
75. Khan, A.Q.; Ghaffar, B.; Shah, M.; Ullah, I.; Oliveira-Júnior, J.F.; Eldin, S.M. Possible seismo-ionospheric anomalies associated with the 2016 Mw 6.5 Indonesia earthquake from GPS TEC and Swarm satellites. *Front. Astron. Space Sci.* **2022**, *9*, 1065453. [CrossRef]